Journal Pre-proof

Closing a biorefinery cycle of giant reed through the production of microporous and reusable activated carbon for CO$_2$ adsorption

Nicola Di Fidio, Domenico Licursi, Monica Puccini, Sandra Vitolo, Anna Maria Raspolli Galletti
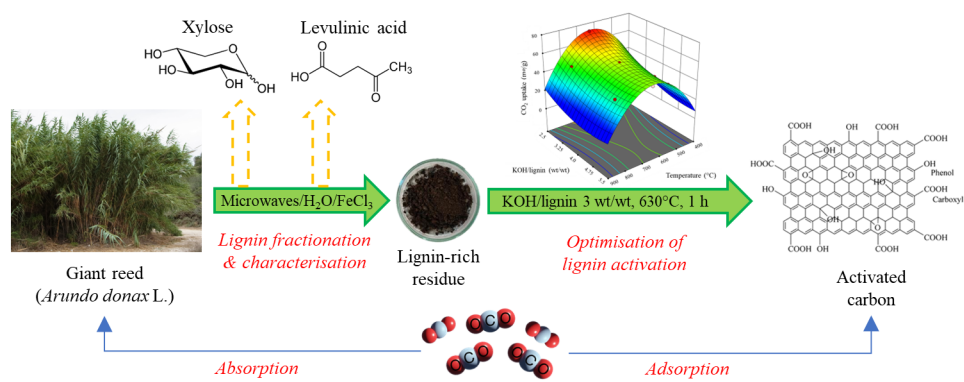
Please cite this article as: Di Fidio N, Licursi D, Puccini M, Vitolo S, Raspolli Galletti AM, Closing a biorefinery cycle of giant reed through the production of microporous and reusable activated carbon for CO$_2$ adsorption, *Journal of Cleaner Production* (2023), doi: https://doi.org/10.1016/j.jclepro.2023.139359.

Xylose

Levulinic acid

Microwaves/H₂O/FeCl₃

Lignin fractionation & characterisation

Giant reed (*Arundo donax* L.)

Lignin-rich residue

KOH/lignin 3 wt/wt, 630°C, 1 h

Optimisation of lignin activation

Activated carbon

COOH   OH   COOH   COOH
HOOC   OH   Phenol
HO   O   C=O   HO   COOH   Carboxyl
                              O
COOH   OH   O   COOH

Absorption

Adsorption

Closing a biorefinery cycle of giant reed through the production of microporous and reusable activated carbon for CO$_2$ adsorption

Nicola Di Fidio[a]*, Domenico Licursi[a], Monica Puccini[b], Sandra Vitolo[b], Anna Maria Raspolli Galletti[a]

[a]Department of Chemistry and Industrial Chemistry, University of Pisa, Via G. Moruzzi 13, Pisa, Italy

[b]Department of Civil and Industrial Engineering, University of Pisa, Largo Lucio Lazzarino, Pisa, Italy

*Corresponding author: Nicola Di Fidio

E-mail address: nicola.difidio@unipi.it

Telephone: +39 0502219210

ABSTRACT

The complete valorisation of all biomass components represents a crucial strategy for developing new biorefinery schemes. This study completed a cascade biorefinery process for the exploitation of holocellulose and lignin fractions of the non-food biomass giant reed (*Arundo donax* L.). The residual lignin-rich solid fraction, obtained after the selective conversion of hemicellulose and cellulose fractions to valuable bioproducts, was characterised and activated by KOH treatment into microporous activated carbon (AC), to be proposed for CO$_2$ adsorption. The production of AC was optimised by the Design of Experiments technique. Under the optimised process conditions (630 °C, KOH/lignin 3.0

26 wt/wt, 60 min) the AC yield was 34.4 wt% and the CO_2 uptake reached 72.3 mg/g,

27 confirming the promising application of this biomaterial. Moreover, the obtained AC

28 showed similar CO_2 uptake values over 10 cycles of adsorption/desorption tests,

29 demonstrating its good recyclability, keeping its pristine CO_2 uptake capacity.

30

31 **Keywords:** Biorefinery; *Arundo donax* L.; lignin-rich residue; activated carbon; CO_2

32 capture.

33

34 **1. Introduction**

35 The development of new biorefinery processes based on the complete exploitation of

36 renewable resources, such as lignocellulosic biomass, is crucial for achieving most of the 17

37 Sustainable Development Goals defined by the United Nations (United Nations, 2023). The

38 selective fractionation and conversion of the biomass components via chemical and/or

39 biological routes allow the synthesis of biofuels, green solvents, biomaterials, and fine

40 chemicals, to propose in substitution of fossil-based ones (Raspolli Galletti *et al.*, 2021). A

41 sustainable solution to overcome the ethical contrast "food versus fuel" consists of the use of

42 waste or non-edible biomasses cultivated on marginal or polluted soils (Viccaro *et al.*, 2022).

43 Among non-edible crops, giant reed (*Arundo donax* L.) represents a suitable renewable

44 material for developing new biorefinery schemes, since it is a perennial grass characterised by

45 high production yield, even on marginal, contaminated, or underutilised lands, low water

46 demand, high polysaccharide content and good resistance to several pathogens (Pilu *et al.*,

47 2014; Scordia and Cosentino, 2019). Traditional biorefinery processes generally produce a

48 lignin residue as the main side-stream, which is usually burned to produce energy with low

49 efficiency. However, lignin represents a renewable source of aromatic compounds (Di Fidio

50 *et al.*, 2021b) or can be advantageously exploited through the production of new biomaterials,

2

51 including activated carbon (AC) (Sellaoui *et al.*, 2023). ACs can be proposed for the

52 adsorption of polluting gases, such as carbon dioxide, organic compounds (Allahkarami,

53 Esmaeil *et al.*, 2023b; Nandi *et al.*, 2023; Xing *et al.*, 2023) and polluting cations/anions in

54 aqueous solutions, such as Ni(II), Cu(II), nitrate, etc. (Allahkarami, Ebrahim *et al.*, 2022;

55 Allahkarami, Ebrahim *et al.*, 2023). The most common biorefinery models of lignocellulosic

56 biomasses are currently developed on the cellulose exploitation, paying much lower attention

57 to the contemporary valorisation of hemicellulose and lignin fractions.

58 Bio-based microporous AC has attracted much interest in recent years since it represents a

59 sustainable and efficient adsorbent for the development of a plethora industrial applications. It

60 is a suitable alternative to traditional adsorbents, such as organic-inorganic hybrid sorbents,

61 zeolites, microporous polymers, and metal-organic frameworks, due to its several advantages,

62 such as low cost, high availability, high surface area, hydrophobicity, easy recyclability, and

63 low energy requirement for the regeneration of the pristine properties (Azmi *et al.*, 2022; Guo

64 *et al.*, 2023). In particular, the wastewater treatment (WWT) of municipal and industrial

65 effluents, and the adsorption of polluting gases represent two of the most studied AC

66 applications. ACs are used within WWT processes due to their high efficiency in adsorbing

67 several kinds of toxic pollutants, such as phenol and heavy metals (Allahkarami, Esmaeil *et*

68 *al.*, 2023b; Rezai and Allahkarami, 2021). Remarkably, innovative ACs functionalised by

69 magnetic metals have been recently employed for phenol removal from aqueous solutions, by

70 this way improving the AC adsorption efficiency and its next recovery/reuse (Allahkarami,

71 Esmaeil *et al.*, 2022, 2023a).

72 Unfortunately, pure lignin and lignin-rich residues are generally characterised by a very

73 low surface area, due to their macroporous or non-porous structure, thus hampering their

74 efficient employment for adsorption uses. For this reason, a physico-chemical activation step

75 is necessary for obtaining a microporous and functionalised texture, which is a highly

76   desirable property for industrial applications (Alcañiz-Monge *et al.*, 2022; Heidarinejad *et al.*,

77   2020; Supanchaiyamat *et al.*, 2019). Chemical activation offers significant advantages with

78   respect to the physical one, since the former allows the choice of different precursors and

79   activating agents to produce ACs in high yields and with better tailored surface properties

80   (Alcañiz-Monge *et al.*, 2022). Furthermore, CO_2 uptake is strictly related to the basicity of AC

81   as well as to the activation conditions used for the biomass thermal processing (Malini *et al.*,

82   2023).

83   The present work deals with an innovative thermochemical valorisation of the lignin-rich

84   residue recovered at the end of a cascade process previously optimised by us for the raw

85   *Arundo donax* L. (Di Fidio *et al.*, 2019; Di Fidio *et al.*, 2020a). This carbon-rich biomaterial

86   was selected as the precursor for AC production, representing the final waste of the cascade

87   process developed for the tailored valorisation of polysaccharides, and its further valuable

88   exploitation was proposed in the perspective of the Circular Economy criteria. In this context,

89   the present biorefinery scheme aims at closing the circle of the complete and profitable

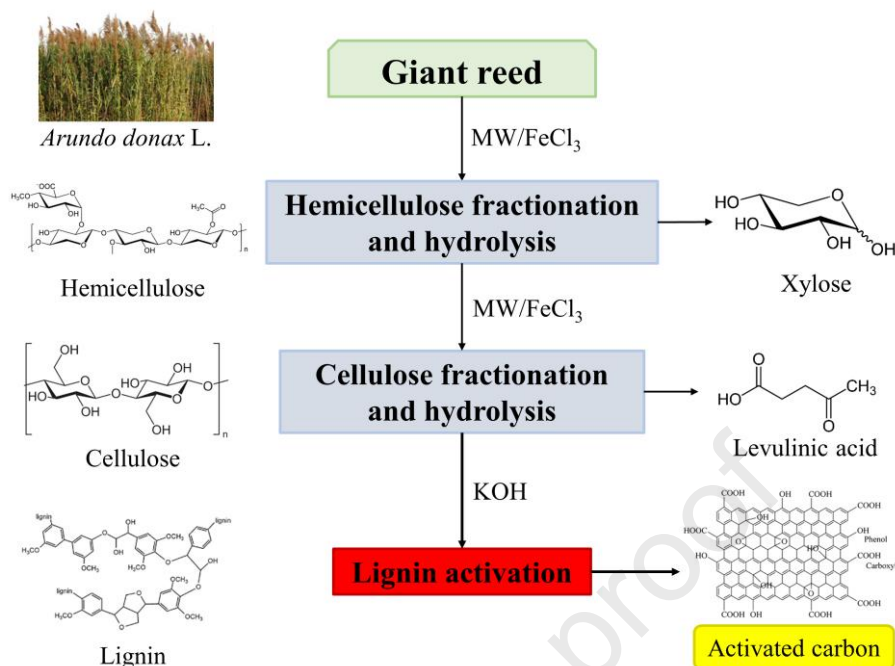90   exploitation of the starting renewable material (Fig. 1).

91

92

93 **Fig. 1**

94

95   Figure 1 shows the schematic representation of the cascade biorefinery implemented to

96 obtain valuable polysaccharide derivatives and the lignin-rich residue, which was used in this

97 work as the precursor for the production of ACs suitable for CO_2 adsorption. A tailored

98 conversion of the holocellulose was optimised in our previous works. In the first step, the

99 conversion of hemicellulose catalysed by $FeCl_3$ under microwave (MW) irradiation co-

100 produced xylose and a solid residue enriched in cellulose. The latter was then used as the

101 feedstock for the subsequent conversion of glucan to levulinic acid and formic acid catalysed

102 again by $FeCl_3$ under MW irradiation, but working under harsher reaction conditions (Di

103 Fidio *et al.*, 2019; Di Fidio *et al.*, 2020a). This final lignin-rich residue represents the starting

104 feedstock to produce AC, by using KOH as the activating agent. The process conditions for

105 this activation treatment have been optimised by adopting the Design of Experiments (DoE)

106 technique based on the Response Surface Modelling (RSM). The process implementation has

107 been devoted to obtaining ACs characterised by tailored surface properties, mainly in terms of

108 specific surface area and porosity, both highly desirable to achieve the best CO_2 adsorption.

109   In the literature, only a few works investigated the production of ACs directly from the raw

110 giant reed (Bhattarai *et al.*, 2022; Singh *et al.*, 2017a; Singh *et al.*, 2017b; Üner, 2019) while,

111 up to now, no study considered the AC production from this lignin stream originating from

112 such a biorefinery process. Moreover, in the literature, only two studies described the

113 adsorption performances of AC produced by giant reed for CO_2 capture (Singh *et al.*, 2017a;

114 Singh *et al.*, 2017b). Based on all these considerations, the main objectives of the present

115 work were: (i) the preliminary characterisation of the starting precursor, namely the lignin-

116 rich residue; (ii) the optimisation of the thermochemical activation of this precursor to give

117 ACs with prevailing microporosity; (iii) the optimisation of the CO_2 uptake and the evaluation

118 of the recycling of the most performing AC.

119

120 **2. Materials and methods**

121

122 *2.1 Biomass and reagents*

123

124   *Arundo donax* L. was obtained from a mature 4-year-old plantation at the Centre for Agri-

125 environmental Research "Enrico Avanzi" of the University of Pisa, located in San Piero a

126 Grado (Pisa, Italy). Culms and leaves were mixed and ground into particles of approximately

127 1.0 mm in size, then dried at 105 °C in an oven and stored in a desiccator until their

128 utilisation. All the used chemicals were provided by Sigma-Aldrich, with the following purity

129 degrees: water for HPLC, iron(III) chloride hexahydrate (>97%), sulfuric acid (98%),

130 hydrochloric acid (37%), potassium bromide (≥99%), sodium hydroxide (≥98%), potassium

131 hydroxide (90%). All reagents were used as received.

132

133 *2.2 Chemical composition of biomass samples*

6

134

135   The chemical composition of the raw biomass and all the solid streams originating within

136   the proposed biorefinery process was determined by the standard NREL methods (Sluiter *et*

137   *al.*, 2008). Each sample was analysed three times.

138

139   *2.3 Microwave-assisted catalytic conversion*

140

141   The Discover S-class microwave reactor (CEM company) was used to perform the two-

142   step hydrolysis process of holocellulose. For the selective hydrolysis of hemicellulose to give

143   xylose, catalysed by the homogeneous Lewis acid $FeCl_3$, the previously optimised reaction

144   conditions were 1.5 wt% $FeCl_3$, 150 °C, 2.5 min, and 9 wt% of biomass loading (Di Fidio *et*

145   *al.*, 2019). Subsequently, for the synthesis of levulinic and formic acid from the acid-

146   pretreated substrate, the previously optimised process conditions were 190 °C, 15 min, 2.2

147   wt% $FeCl_3$, and 9 wt% of biomass loading (Di Fidio *et al.*, 2019; Di Fidio *et al.*, 2020a).

148

149   *2.4 Elemental analysis*

150

151   An automatic analyser Vario MICRO Cube (Elementar), equipped with a thermal

152   conductivity detector, was used for the elemental analysis (C, H, N, S) of raw giant reed,

153   lignin-rich residue, and AC samples. The oxygen content of the samples was calculated

154   through the equation 1:

155   O (wt%) = 100 (wt%) – (C (wt%) + H (wt%) + N (wt%) + S (wt%) + ash (wt%))   (1)

156

157   *2.5 Infrared spectroscopy*

158

7

159   A Perkin–Elmer "Spectrum Two" spectrophotometer was used for the acquisition of IR

160   spectra in transmission mode (KBr pellet method) and Attenuated Total Reflection (ATR)

161   mode. In the first case, 0.5 mg of sample was mixed with 400 mg of KBr. Then 120 mg of the

162   mixture was used for the preparation of the pellet having a thickness of 200 ± 10 μm. In the

163   second case, the same instrument was equipped with an attenuated total reflectance apparatus.

164   All the IR spectra were acquired through 24 scans in the range 4000-450 cm^{-1} with a nominal

165   resolution of 8 cm^{-1}. ATR-FTIR was used for the characterisation of the raw material and

166   lignin-rich residue (our precursor of ACs), while the transmission mode (FTIR) was used for

167   the characterisation of ACs due to their very low transmittance.

168

169   *2.6 Size-exclusion chromatography (SEC)*

170

171   SEC was performed on the soluble fraction of the lignin-rich residue (accounting for 67

172   wt%) in an alkaline solution (0.5 M NaOH), which was used as the solvent/eluent, according

173   to the method proposed by Constant *et al.* (Constant *et al.*, 2016). Poly(styrene sulphonate)

174   sodium salt standards (M_w range 891-258000 g/mol) were used for the calibration.

175

176   *2.7 Synthesis of ACs*

177

178   The DoE was performed according to the RSM, and it was exploited to optimise the AC

179   synthesis from the lignin-rich residue. Activation temperature (A) and KOH/lignin weight

180   ratio (B) were selected as the independent variables, namely the factors (Table 1). The

181   reaction time was fixed at 60 min. For each factor, two levels (low and high) were selected,

182   according to Table 1.

183

184   **Table 1.** Independent variables (factors) and levels of the experimental design.

Factor	Name	Unit	Low	High
A	Temperature	°C	500	800
B	KOH/lignin	wt/wt	3	5

185

186   The responses (dependent variables) selected to monitor the AC synthesis were: i) AC yield

187   (wt%); ii) carbon yield (wt%); iii) CO_2 uptake (mg/g). They were calculated by the following

188   equations:

189   Y_{AC} (wt%) = $(m_{AC}/m_{lignin}) \times 100$ (2)

190   Y_C (wt%) = $Y_{AC} \times (C\%_{AC}/C\%_{lignin})$ (3)

191   CO_2 uptake (mg/g) = m_{CO2}/m_{lignin} (4)

192   where Y_{AC} is the AC yield, m_{AC} is the mass of recovered AC, m_{lignin} represents the mass of the

193   lignin-rich residue, Y_C is the carbon yield, $C\%_{AC}$ and $C\%_{lignin}$ represent the carbon content in

194   the AC and the lignin-rich residue, respectively, determined by elemental analysis, m_{CO2} is the

195   mass of CO_2 determined by TGA in the adsorption tests.

196   For the AC synthesis, the lignin-rich residue (powder) was mixed with potassium

197   hydroxide flakes, by using an agate mortar. According to the B factor data of the DoE, 1 g of

198   the lignin-rich residue was mixed with a proper amount of KOH, until reaching a

199   homogenous solid mixture. For each run of the DoE, 1.25 g of the KOH/lignin mixture was

200   transferred into an alumina cup, which was subsequently placed in a tubular reactor and

201   heated under N_2 atmosphere (flow of 100 mL/min). The activation temperature was defined

202   according to each run of the experimental design. The heating/cooling rate of 5 °C/min was

203   adopted in all the tests. The solid stream recovered after pyrolysis was washed with 20 mL of

204   2 M HCl solution to remove the excess of KOH and with deionized water up to neutrality. AC

205   was dried at 105 °C up to constant weight and stored in a desiccator before its use.

206

2.8 Thermogravimetric analysis (TGA)

208

209   The TGA of the pristine precursor and the corresponding AC was carried out by using a

210   TGA Q500 TA Instrument. The alumina crucible containing ca. 10 mg of the sample was

211   dynamically heated, according to the following operating conditions: i) 20 °C/min from 30 to

212   105 °C under a constant flow of N_2 (100% v/v); ii) 105 °C for 10 min to determine the

213   humidity content of the sample; iii) 20 °C/min from 105 to 900 °C under a constant flow of

214   N_2 (100% v/v); iv) 900 °C for 10 min to determine the content of organic compounds; v)

215   cooling from 900 to 800 °C under an air/N_2 mixture flow (air 60% v/v, N_2 40% v/v); vi) 800

216   °C for 20 min to determine the ash content and the fixed carbon content (by difference).

217

2.9 CO_2 adsorption/desorption tests

219

220   The CO_2 adsorption/desorption properties of ACs were evaluated using the TGA Q500,

221   TA Instrument. A schematic diagram of the experimental apparatus was reported in Figure

222   S1. The alumina crucible containing ca. 10 mg of the sample was dynamically heated under

223   the following operating conditions: i) 20 °C/min from 27 to 105 °C under a constant flow

224   (100 mL/min) of N_2 (100% v/v); ii) 105 °C for 10 min to remove the sample humidity; iii)

225   from 105 to 27 °C under a constant flow (100 mL/min) of N_2 (100% v/v). The adsorption test

226   was performed by treating the sample at 27 °C for 20 min under a 100 mL/min flow

227   containing CO_2 60% v/v and N_2 40% v/v. After reaching the plateau, the gas flow was

228   switched to 100 vol% N_2 (constant flow of 100 mL/min) and CO_2 desorption took place. Both

229   during adsorption and desorption tests, the sample weight variation was acquired as a function

230   of the time (Licursi *et al.*, 2023).

231

232   *2.10 Analysis of specific surface area, pore volume and size distribution*

233

234   Multi-point determination of specific surface area, pore volume and size distribution of AC

235   produced under different activation conditions was performed by ALFAST company. N_2

236   adsorption/desorption isotherms were obtained at -196 °C by a 3Flex Adsorption Analyzer

237   (Micrometrics). Before the analysis, a pretreatment was conducted for 180 min at 200 °C

238   under a constant flow of N_2 (100% v/v), aimed at the humidity removal. The specific surface

239   area of each AC was determined through the Brunauer-Emmet-Teller (BET) method, while

240   the nonlocal density functional theory (NLDFT) was adopted for the determination of

241   micropore size distribution, according to the literature (Jagiello *et al.*, 2015). The BET

242   specific surface area was evaluated taking into account the Rouquerol's theory (Rouquerol *et*

243   *al.*, 2007), which is effective for extending BET analysis to microporous materials. In this

244   context, each microporous sample reveals an optimal range for the application of the BET

245   fitting. In the present study, the adopted range for ACs obtained in runs 3, 6 and under the

246   optimised conditions was withing 0.01-0.06 p/p^0, whilst for the AC obtained in run 2, it was

247   0.02-0.15 p/p^0. In all the performed analyses, the pressure ranges shifted downward from the

248   typical range of the BET method, namely 0.05-0.35 p/p^0, which is notoriously an unsuitable

249   range for microporous samples (Maziarka *et al.*, 2021). Moreover, the Dubinin-Radushkevich

250   model was employed for the fitting of type I isotherms.

251

252   *2.11 Scanning electron microscopy (SEM)*

253

254   For high-resolution imaging purposes, the SEM analysis was carried out by a FEI

255   QUANTA 450 ESEM-FEG microscope, which operates in low vacuum mode, with a

256   chamber vacuum pressure ranging from 10-130 Pa. At 30 kV, it enables a nominal electron

257   beam resolution of 1.4 nm.

258

259   *2.12 Raman spectroscopy analysis*

260

261   The lignin-rich residue and AC obtained under the optimised reaction conditions were

262   analysed by Raman spectroscopy. Raman spectra were acquired by using a Renishaw inVia

263   confocal micro-Raman system, connected to a Leica DLML microscope equipped with a

264   NPLAN objective (50×) having a numerical aperture of 0.75. The laser source was a Ng-YAG

265   laser emitting at 532 nm, having a spectral resolution of 2.0 cm^{-1}. Positions of D and G band,

266   FWHM and I_{DG} ratios were obtained by fitting and integrating the individual peaks with the

267   Lorentzian function via OriginPro2023 software (R^2 value of fittings was higher than 0.98).

268

269   **3. Results and discussion**

270

271   *3.1 Characterisation of the AC precursor*

272

273   *3.1.1 Analysis of chemical composition*

274   The proposed fractionation route was developed according to a previously optimised

275   approach, employing $FeCl_3$ as the acid catalyst and MW heating, as summarised in Figure 1

276   (Di Fidio *et al.*, 2019; Di Fidio *et al.*, 2020a). Inorganic salts are finding widespread use as

277   green catalysts for the production of sugars, organic acids and/or furan derivatives from

278   biomasses (Asada *et al.*, 2020; Loow *et al.*, 2015). Among them, $FeCl_3$ showed excellent

279   catalytic performances for the production of monosaccharides, levulinic acid and 5-

280   hydroxymethylfurfural from lignocellulosic and starchy biomasses (Di Fidio *et al.*, 2020a; Iris

281 *et al.*, 2017). The use of MW as the heating system improves the sustainability and efficiency

282 of the proposed biorefinery scheme because it significantly reduces the reaction time and the

283 energy consumption (Horikoshi *et al.*, 2017; Priecel and Lopez-Sanchez, 2018).

284 The chemical composition of the raw giant reed and the corresponding lignin-rich residue

285 (constituting 21-23 wt% of the initial biomass weight, on a dry basis) obtained through the

286 proposed two-step hydrolysis, is presented in Table 2.

287

288 **Table 2.** Chemical composition (wt%, on a dry basis) of raw *Arundo donax* L. and lignin-rich

289 residue, originating from the proposed two-step hydrolysis.

Fraction	Raw *Arundo donax* L.	Lignin-rich residue
Glucan	36.3	2.6
Xylan	17.3	-
Arabinan	1.9	-
Mannan	0.6	-
Acetyl groups	3.6	-
Ash	2.0	2.9
Extractives	13.5	-
Protein	1.9	1.3
Acid-insoluble lignin	22.0	93.2
Acid-soluble lignin	0.9	-

290

291 The final lignin-rich residue was characterised by an almost negligible cellulose content (ca.

292 2.5 wt%) and a high lignin content (ca. 93 wt%), confirming the efficiency of the proposed

293 catalytic approach for the selective cascade fractionation of the three main fractions of the

294 lignocellulosic biomass.

295

3.1.2 ATR-FTIR spectroscopy

297 ATR-FTIR spectroscopy (Fig. S2) corroborated the fractionation of the hemicellulose,

298 cellulose and lignin fractions. The absorption band at 3330 cm^{-1} is due to the stretching of the

299 O-H group (Fiore *et al.*, 2014), whose intensity reached its minimum in the lignin-rich

300 residue, according to the disappearance of the holocellulose and the chemical condensation of

301 aromatic structures characterising the lignin structure. The two absorption bands at 2920 and

302 2850 cm^{-1} are due to the C-H stretching vibrations of -CH$_2$ / -CH$_3$ and O-CH$_3$, respectively

303 (Chen *et al.*, 2019). The absorption band at 1732 cm^{-1} is due to the C=O stretching vibrations

304 of unconjugated ketone, carbonyl, and ester groups and it is ascribable to the acetyl groups of

305 the hemicellulose fraction (Fiore *et al.*, 2014). Its presence in the raw *Arundo donax* L. and its

306 absence in the lignin-rich residue confirmed the successful hydrolysis of the hemicellulose

307 component, as a consequence of the first hydrolysis step. Conversely, the absorption bands at

308 1701 and 1596 cm^{-1}, ascribed to the stretching of C=O conjugated to the aromatic rings of

309 lignin and to the aryl ring symmetric stretching of aromatic skeletal in lignin, respectively

310 (Chen *et al.*, 2019), were sharper in the lignin-rich residue. Moreover, the absorption band at

311 1510 cm^{-1} is assessed to the asymmetric aryl ring stretching, that at 1459 cm^{-1} to the

312 asymmetric C-H deformation, that at 1210 cm^{-1} to the C-C and C-O stretching, and that at

313 1110 cm^{-1} to the aromatic C-H in-plane deformation (Di Fidio *et al.*, 2020b). Lastly, C-O

314 stretching vibrations of hydroxyl and ether groups of cellulose are visible at 1033 cm^{-1} (Fiore

315 *et al.*, 2014).

316

3.1.3 Elemental analysis

318   The bulk removal of hemicellulose and cellulose from the *Arundo donax* L. biomass was

319   also confirmed by elemental analysis. Data related to the raw biomass and the lignin-rich

320   residue are reported in Table 3.

321

322   **Table 3.** Elemental analysis of raw *Arundo donax* L. and lignin-rich residue.

Run	C (wt%)	H (wt%)	N (wt%)	O* (wt%)	H/C atomic ratio	O/C atomic ratio
Raw *Arundo donax* L.	46.4	5.8	0.3	45.4	1.5	0.7
Lignin-rich residue	62.0	4.8	0.2	28.6	0.9	0.3

323   * O (wt%) = 100 (wt%) – (C (wt%) + H (wt%) + N (wt%) + S (wt%) + ash (wt%))

324

325   Carbon and oxygen contents of the lignin-rich residue were 62.0 and 33.0 wt%, respectively.

326   These findings are consistent with previously reported literature data for major commercial

327   lignin types, including Kraft lignin Indulin® AT, Soda Protobind™ 1000, and Alcell™

328   organosolv lignin (Constant *et al.*, 2016).

329

330   ***3.1.4 SEC of the alkaline-soluble lignin***

331   The molecular weight of the lignin-based precursor can significantly influence the pore

332   ordering of the obtained AC (Qin *et al.*, 2018). The molar mass distribution of the alkaline-

333   soluble fraction of the lignin-rich residue (67 wt%) was determined by SEC (Fig. S3). The

334   number average molecular weight (M_n) was 804 g/mol, while the weight average molecular

335   weight (M_w) was 2252 g/mol. The polydispersity index (M_w/M_n) was 2.8, thus indicating a

336   broad distribution of the biopolymer chains. These results agreed with those previously

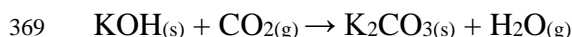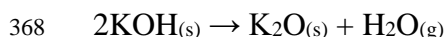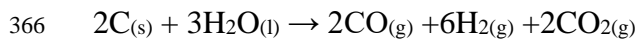337   reported for *Arundo donax* L.-derived lignins (You *et al.*, 2013) as well as for other
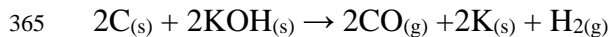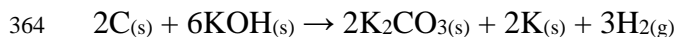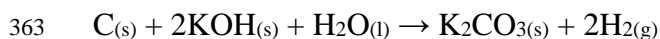
15

338   commercial lignins (Constant *et al.*, 2016). Remarkably, such alkaline-soluble lignin fraction

339   could be separately exploited for the synthesis of even more added-value bio-carbons, such as

340   ordered mesoporous carbons, by soft-template methods (Qin *et al.*, 2018), opening the way to

341   further valorisation routes of this residue towards various valuable chemicals and materials.
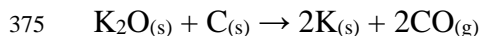
342

343   *3.2 Synthesis and characterisation of AC starting from the lignin-rich residue*

344

345   According to the literature, several activation methods are available, including steam

346   activation and carbonisation coupled with gas activation, considered as physical activation

347   methods, or chemical activation ones, requiring the impregnation with a chemical activating

348   agent, such as KOH, H_3PO_4, $ZnCl_2$ (Azmi *et al.*, 2022; Malini *et al.*, 2023). There are also

349   studies on MW-assisted activation, such as MW-assisted pyrolysis and hydrothermal

350   carbonisation (HTC) (Kaur *et al.*, 2021; MacDermid-Watts *et al.*, 2021). All these methods

351   can lead to ACs with different surface properties (mainly in terms of specific surface area and

352   pore size distribution) and chemical composition. The choice of the most appropriate

353   activation method depends on several factors: first of all, the final application of the AC and,

354   secondly, the kind of the precursor (Licursi *et al.*, 2023). In the present work, the lignin-rich

355   residue was used as the precursor to produce cheap AC, resulting in efficient CO_2 adsorption.

356   KOH activation is effective for the synthesis of microporous AC with a high capacity for CO_2

357   adsorption (Nandi *et al.*, 2023; Singh *et al.*, 2017a). In this context, ACs from KOH activation

358   are characterised by a high surface area and narrow pore size distribution (Malini *et al.*, 2023;

359   Xing *et al.*, 2023). The solid-to-solid reaction is effective for avoiding the carbonatation of

360   KOH, but also for economical and practical reasons. In particular, when KOH reacts with

361   carbon of biomass, K_2CO_3, K, H_2O, H_2, CO_2 and CO are produced, according to the following

362   reactions (Malini *et al.*, 2023; Nandi *et al.*, 2023):

363     $C_{(s)} + 2KOH_{(s)} + H_2O_{(l)} \rightarrow K_2CO_{3(s)} + 2H_{2(g)}$

364     $2C_{(s)} + 6KOH_{(s)} \rightarrow 2K_2CO_{3(s)} + 2K_{(s)} + 3H_{2(g)}$

365     $2C_{(s)} + 2KOH_{(s)} \rightarrow 2CO_{(g)} + 2K_{(s)} + H_{2(g)}$

366     $2C_{(s)} + 3H_2O_{(l)} \rightarrow 2CO_{(g)} + 6H_{2(g)} + 2CO_{2(g)}$

367     $C_{(s)} + CO_{2(g)} \rightarrow 2CO_{(g)}$

368     $2KOH_{(s)} \rightarrow K_2O_{(s)} + H_2O_{(g)}$

369     $KOH_{(s)} + CO_{2(g)} \rightarrow K_2CO_{3(s)} + H_2O_{(g)}$

370 The production of volatiles from the precursor contributes to improve the AC porosity. In

371 addition, the formation of pores is favoured by the following reactions, occurring mainly

372 between biomass carbon and K_2CO_3 or K_2O (Nandi *et al.*, 2023):

373     $K_2CO_{3(s)} + 2C_{(s)} \rightarrow 2K_{(s)} + 3CO_{(g)}$

374     $K_2CO_{3(s)} + 2C_{(s)} \rightarrow K_2O_{(s)} + 2CO_{(g)}$

375     $K_2O_{(s)} + C_{(s)} \rightarrow 2K_{(s)} + 2CO_{(g)}$

376 A chemometric approach based on the RSM was adopted to optimise the main process

377 parameters of the lignin activation step (Table 4). The experimental (full-factorial

378 randomised) test plan is shown in Table 4, including 10 total runs, with 4 runs at factorial

379 points, 4 runs at axial points, and 2 replicates at the central point of the design, according to

380 equation 5:

381     $N_{runs} = 2^n + 2n + n_c$ (5)

382 where N_{runs} is the number of total experimental runs required for a full-factorial central

383 composite design (CCD), n is the number of independent factors, $2n$ is the number of axial

384 runs and n_c is the number of runs conducted at the centre of the design. The CCD alpha value

385 (α), which represents the distance of axial points from the centre of the design space, was set

386 to 1.414 to obtain a rotatable design (Table 4).

387

17

388   **Table 4.** Experimental design matrix (process time 60 min).

Run	T (°C)	KOH/lignin weight ratio (wt/wt)
1	862.1	4.0
2	800.0	3.0
3	650.0	2.6
4	800.0	5.0
5	437.9	4.0
6	500.0	3.0
7	650.0	5.4
8	650.0	4.0
9	500.0	5.0
10	650.0	4.0

389

390   The TGA curves of the precursor and ACs were acquired (Fig. S4) while the

391 corresponding proximate analysis data are reported in Table 5.

392

393 **Table 5.** Proximate analysis data of precursor and ACs.

Run	Volatiles (wt%)	Fixed carbon (wt%)	Ash (wt%)
Lignin-rich residue	55.3	40.3	4.4
1	7.9	78.1	14.0
2	19.6	62.3	18.1
3	28.0	66.9	5.1
4	9.2	86.3	4.5
5	35.8	55.6	8.6
6	37.4	58.7	3.9

18

7	14.8	74.0	11.2
8	23.4	71.3	5.3
9	50.7	42.6	6.7
10	20.5	74.3	5.2

394

395

All the ACs produced under less severe conditions (≤ 500 °C), such as those obtained from run 5 (437.9 °C, 4.0 KOH/lignin), run 6 (500 °C, 3.0 KOH/lignin) and run 9 (500 °C, 5.0 KOH/lignin), showed the lowest fixed carbon content, which was comparable with that of the pristine lignin-rich residue (40 wt%). On the contrary, ACs synthesised at higher temperatures (≥ 650 °C) were characterised by a higher content of fixed carbon, confirming the advanced carbonisation of the lignin-rich precursor. Moreover, most of the ACs showed a lower ash content than the maximum one (10 wt%) allowed for commercial uses (Zulkania et al., 2018).

The results of the elemental analysis of all the AC samples were reported in Table 6.

404

Table 6. Elemental analysis data of lignin-rich residue and synthesised ACs.

Run	C (wt%)	H (wt%)	N (wt%)	O* (wt%)	H/C atomic ratio	O/C atomic ratio
Lignin-rich residue	62.0	4.8	0.2	28.6	0.9	0.3
1	77.6	0.9	0.3	7.3	0.1	0.1
2	76.0	0.4	0.4	5.1	0.1	0.1
3	73.0	3.2	0.1	18.6	0.5	0.2
4	82.4	0.8	0.2	12.1	0.1	0.1
5	59.3	2.8	0.1	29.2	0.6	0.4
6	72.6	3.1	0.1	20.3	0.5	0.2

19

7	74.3	0.8	0.2	13.5	0.1	0.1
8	70.0	3.1	0.1	21.5	0.5	0.2
9	56.1	2.9	0.1	34.1	0.6	0.5
10	72.8	3.0	0.1	18.9	0.5	0.2

406 * O (wt%) = 100 (wt%) – (C (wt%) + H (wt%) + N (wt%) + S (wt%) + ash (wt%))

407

408 The H/C and O/C atomic ratios were reported in the van Krevelen diagram, which is useful

409 for depicting the progress of the carbonisation progress, highlighting some details about the

410 corresponding mechanism (Fig. 2).

411
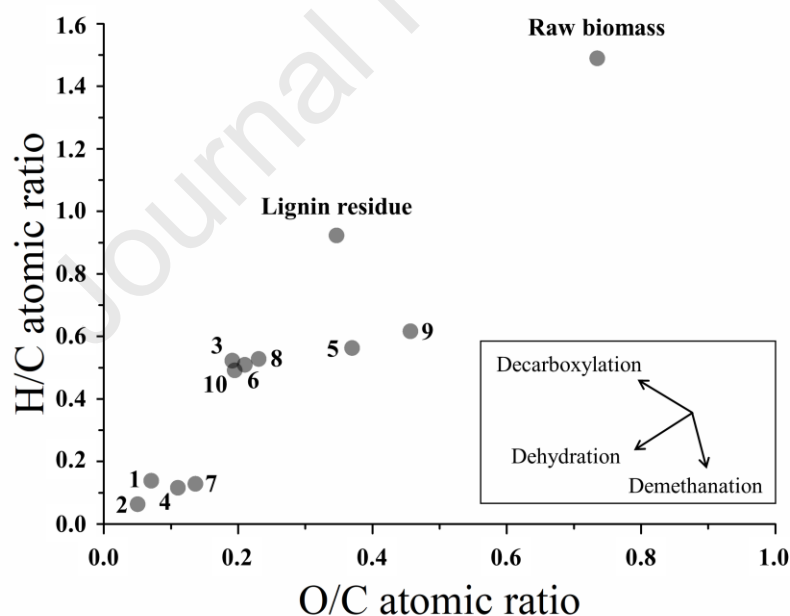
412

413 **Fig. 2**

414

415 The distribution of the H/C and O/C atomic ratios in the Van Krevelen diagram demonstrated

416 that dehydration reaction was the prevailing path involved in the production of both lignin-

417 rich residue and ACs. The ACs obtained at high temperatures (≥ 650 °C) were characterised

20

418 by lower H/C and O/C atomic ratios, while those obtained under less severe conditions ($\leq$ 500

419 °C), such as ACs obtained from runs 5 and 9, showed higher O/C values.

420   FTIR spectra of ACs obtained in runs 1-10 were acquired (Fig. S5). The absorption band in

421 the range of 3100-3500 cm^{-1} is ascribable to the stretching of the O-H bonds. Those in the

422 range 2800-3000 cm^{-1} are related to the C-H stretching vibrations of -CH_2 and -CH_3 groups.

423 The absorption bands in the range 1000-1300 and 1640-1750 cm^{-1} are due to the stretching

424 vibrations of C-O and C=O bonds of ketones, aldehydes and carboxylic acids, as well as

425 phenolic esters. The intensity decrease of such absorption bands is related to the occurred

426 removal of volatile organic compounds and the deoxygenation of the pristine material. The

427 band at 1630 cm^{-1} is due to C=C ring stretching vibrations and it is indicative of progress of

428 the biomass carbonisation.

429   The CO_2 uptake of the starting lignin-rich residue, namely the control test, and of the ACs

430 obtained in the runs 1-10 was evaluated (Fig. S6). The AC characterised by the highest CO_2

431 uptake (72.6 mg/g) was obtained from run 3 (650.0 °C, KOH/lignin 2.6 wt/wt, 60 min).

432 Moreover, by comparing the CO_2 adsorption uptake of the pristine lignin-rich residue (6.9

433 mg/g) and the AC, it becomes clear that the activation process significantly improved the

434 adsorption performance. Furthermore, the use of temperatures higher than 800 °C or lower

435 than 500 °C, together with high activating agent ratios ($\geq$ 4 wt/wt), led to lower CO_2 uptakes

436 (runs 1, 4, 5, 9, Table 6). Based on these results, intermediate activation temperatures and low

437 KOH/lignin weight ratios were effective in improving the CO_2 uptake capacity of the ACs.

438 Table 7 summarised the values of each response variable achieved in all the runs performed in

439 the RSM analysis.

440

441   **Table 7.** Experimental data of selected response variables.

Run	AC yield (wt%)	Carbon yield (wt%)	CO_2 uptake (mg/g)

Control[*]	-	-	6.9
1	6.4	8.0	17.4
2	18.3	22.4	47.0
3	25.6	30.1	72.6
4	6.2	8.2	40.0
5	16.3	15.6	27.8
6	22.1	25.8	48.9
7	18.2	21.9	49.5
8	20.5	23.1	55.2
9	19.2	17.4	36.3
10	19.0	22.3	54.3

442   * Control test: pristine lignin-rich residue.

443

444   A mathematical model was obtained for each response variable describing the experimental

445   domain. All the obtained models were characterised by a regression square value (R^2) higher

446   than 0.96 and a not-significant Lack of Fit (p-value > 0.1). The analysis of variance

447   (ANOVA) was performed, and corresponding data were reported in Tables S1-3. Figure 3

448   shows the 3D surfaces for AC and carbon yields and CO_2 uptake, respectively, as a function

449   of the investigated process conditions.

450

(A)

(B)

(C)

451
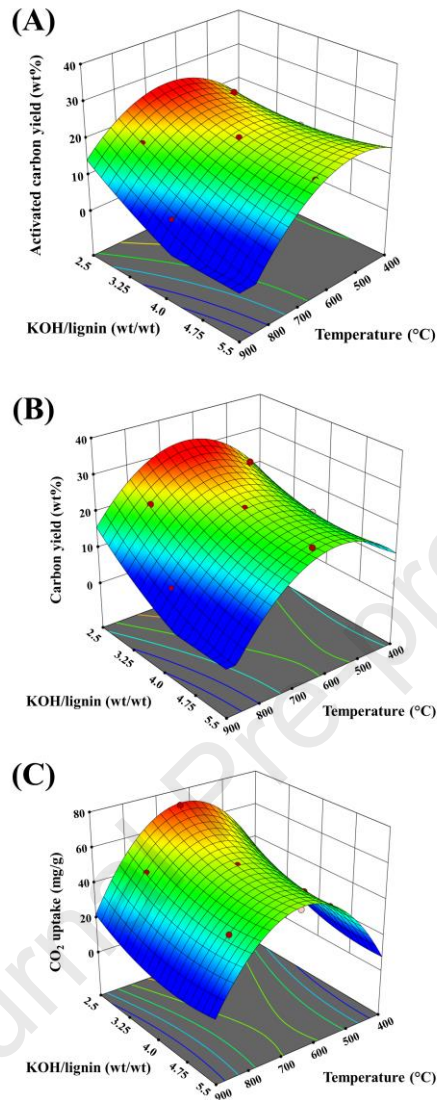
Fig. 3

453

454 The coded model equations related to the AC yield (wt%), carbon yield (wt%) and CO_2

455 uptake (mg/g) are the following:

456 $Y_{AC}(wt\%) = 19.75 - 3.85 \times A - 3.18 \times B - 2.30 \times A \times B - 4.24 \times A^2 + 1.03 \times B^2$ (6)

457 $Y_C(wt\%) = 22.70 - 2.92 \times A - 4.27 \times B - 1.45 \times A \times B - 5.56 \times A^2 + 1.54 \times B^2$ (7)

458 $Y_{CO2}(mg/g) = 54.75 - 1.61 \times A - 6.53 \times B + 1.40 \times A \times B - 15.77 \times A^2 + 3.46 \times B^2$ (8)

459 The prediction of the optimal process conditions was subsequently carried out, aimed at

460 simultaneously maximising the AC yield, the carbon yield, and the CO_2 uptake. The predicted

23

461 optimal conditions were found, corresponding to an activation temperature of 630 °C and a

462 KOH/lignin weight ratio of 3.0 wt/wt. Under these conditions, the model predicted the AC

463 yield of 24.1 wt%, the carbon yield of 28.6 wt% and the CO_2 uptake of 64.9 mg/g (6.5 wt%).

464 These results were experimentally validated, obtaining an AC yield of 34.4 wt%, a carbon

465 yield of 40.6 wt% and a promising CO_2 uptake of 72.3 mg/g (7.2 wt%), confirming the

466 effectiveness of the proposed model.

467 According to Song *et al.* (Song *et al.*, 2015), commercial AC is characterised by a CO_2

468 adsorption capacity of around 65 mg/g (6.5 wt%) at 1 bar and 25 °C, while biomass-derived

469 ACs show wider CO_2 uptakes, reasonably in the range 49-210 mg/g (Serafin *et al.*, 2017).

470 Thus, our AC produced from the *Arundo donax* L. lignin-rich residue, within the proposed

471 biorefinery scheme, can be advantageously exploited for this application.

472 Raman spectra of starting lignin-rich residue and AC obtained under the optimised reaction

473 conditions were acquired (Fig. 4).

474

475

476   **Fig. 4**
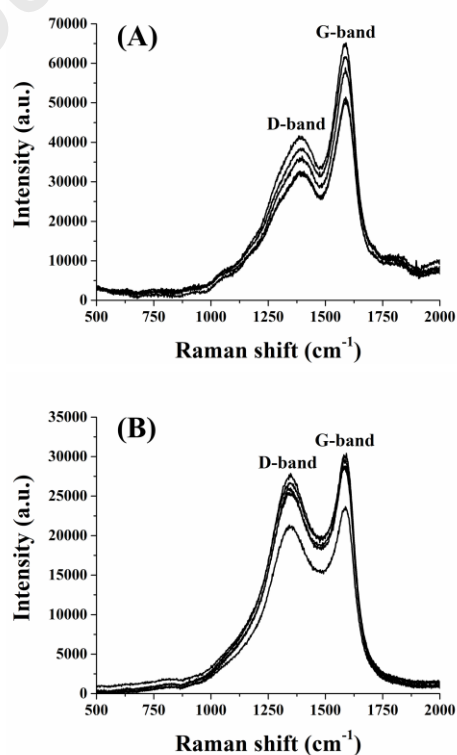
477

478   Raman spectra of disordered and amorphous carbon exhibit two peaks at around 1340-1360

479   cm^{-1} (D-band) and 1570-1600 cm^{-1} (G-band), reflecting the defects in the samples and the

480   ordered sp^2 carbon plane, respectively. The intensity ratio of the D and G band (I_{DG}) is

481   generally considered indicative of the disorder and the graphitization degree of the

482   carbonaceous material, whereas the values for the FWHM reflect the sizes of the domains of

483   the different kinds of carbon structure (Yagmur *et al.*, 2020). The parameters of interest for

484   each deconvoluted spectrum were reported in Table 8.

485

486   **Table 8.** Measured and calculated data from Raman analysis (arithmetic mean value ±

487   standard deviation).

Sample	D pos (cm^{-1})	G pos (cm^{-1})	I_{DG}	FWHM$_D$	FWHM$_G$
Lignin-rich residue	1378±5**	1587±3	0.64±0.02**	248±8*	104±2**
AC	1347±3**	1588±6	0.97±0.02**	264±4*	95±3**

488   *p<0.01; **p<0.001

489

490   The synthesised AC showed a higher I_{DG} value than that of the lignin-rich residue, suggesting

491   the presence of more defects and a disordered graphite-like structure (i.e., a lower

492   graphitization degree). Such a structure may be due to the intercalation of potassium and/or to

493   the presence of oxygenated functional groups. Raman spectra of AC exhibited a strong signal

494   for the D-mode at a decreasing position with respect to the pristine lignin-rich residue, which

495   further confirms the disordered structure of this carbonaceous material. Higher FWHM of the

496   D band was observed for AC, again highlighting its disordered texture. G-band FWHM is

497   often employed to characterise carbon crystallites, and a narrower G-band FWHM implies a

498 reduced presence of bond angle disorder in sp^2 carbons.

499

3.3 Analysis of specific surface area, pore volume and size distribution

501

502 N_2 adsorption isotherm linear plot and BET specific surface area plot at -196 °C of ACs

503 obtained from run 2 (800 °C, KOH/lignin 3.0 wt/wt, 60 min), run 3 (650 °C, KOH/lignin 2.6

504 wt/wt, 60 min), and run 6 (500 °C, KOH/lignin 3.0 wt/wt, 60 min), corresponding to the

505 lowest, the intermediate and the highest temperature selected in the DoE, were compared in

506 Figure 5. Moreover, they were compared with the AC synthesised under the optimised

507 reaction conditions (630 °C, KOH/lignin 3.0 wt/wt, 60 min).

508
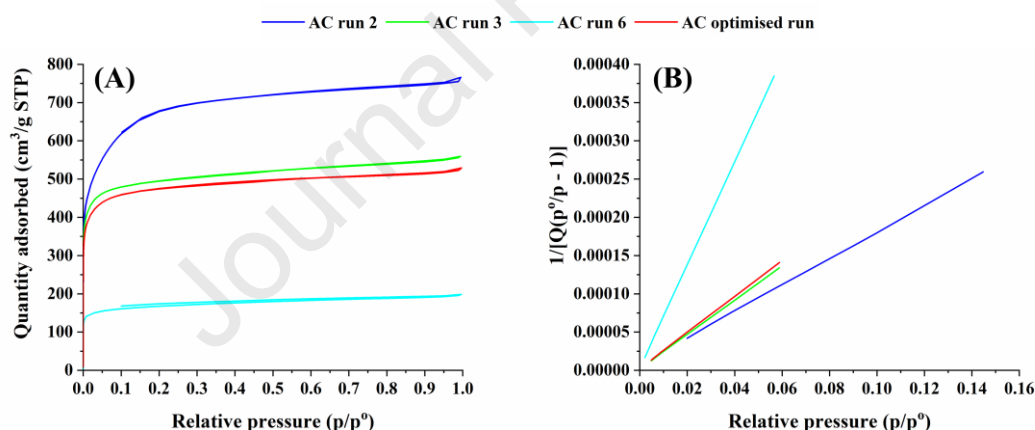
510 **Fig. 5**

511

512 KOH activation promoted the selective formation of micropores, as confirmed by the type I

513 isotherms of these ACs (Fig. 5). AC produced in the run 2 (800 °C, KOH/lignin 3.0 wt/wt)

514 was characterised by significant microporosity and very high specific surface area, that was

515 2507.4 m²/g. This specific surface area was composed of a micropore area of 2369.4 m²/g and

516 an external surface area of 138.0 m²/g. AC obtained from the run 3 (650 °C, KOH/lignin 2.6

517 wt/wt) was also characterised by a microporous texture, with a specific surface area of 1940.4

26

518 m²/g, whereas the micropore area was 1817.1 m²/g and the external surface area was 123.3

519 m²/g. The specific surface area of AC from run 6 (500 °C, KOH/lignin 3.0 wt/wt) was only

520 645.9 m²/g, whereas the micropore area was 587.4 m²/g and the external surface area was 58.5

521 m²/g. These results confirmed that the synthesis of ACs with high microporosity is favoured

522 by higher temperatures, in agreement with the literature (Azmi *et al.*, 2022). The main

523 parameters affecting the microstructure of ACs and, consequently, the N_2 gas sorption results

524 are the type of activating agent, the impregnation ratio, and the activation temperature (Azmi

525 *et al.*, 2022). Regarding the activating agent, the dissolution of ether linkages of lignin-rich

526 materials is facilitated by the utilisation of alkaline chemicals (Malini *et al.*, 2023). Moreover,

527 the application of an activating agent containing potassium generates additional micropores,

528 exploiting the capacity of potassium for expanding the carbon layers. Consequently, this

529 process enhances pore accessibility by breaking down longer fibers, favouring the production

530 of ACs characterised by very high specific surface area and a more uniform distribution of

531 micropores (Singh *et al.*, 2017a). Regarding the impregnation ratio, a reduced concentration

532 of KOH enables a more controlled and stable elimination of volatile matter while preventing

533 the deposition of tar, thus resulting in a greater abundance of micropores (Azmi *et al.*, 2022).

534 Finally, the temperature employed during the activation process of carbon materials plays a

535 crucial role in determining the pore volume, the distribution of pore sizes, the development of

536 microporosity, and the overall specific surface area. Generally, higher temperatures facilitate

537 the removal of moisture and volatile components from the precursor, promoting the further

538 creation of pores (Azmi *et al.*, 2022). However, by increasing the temperature, there is an

539 expected significant decrease in the AC yield, along with the higher concentration of ashes, as

540 reported in Tables 5 and 7.

541   Under the optimised reaction conditions (630 °C, KOH/lignin 3.0 wt/wt), AC showed the

542 specific surface area of 1848.0 m²/g, whereas the micropore area was 1762.8 m²/g and the

543   external surface area was 85.2 m²/g. As expected, these results were quite similar to those

544   achieved from run 3. The specific surface area of 1848.0 m²/g was significantly higher than

545   those obtained for ACs from unpretreated *Arundo donax* L., within the range 500.0-1568.0

546   m²/g (Ahmed, 2016; Singh *et al.*, 2017a). The high specific surface area obtained in the

547   present work further demonstrates the effectiveness of our approach.

548   Figure 6 shows the cumulative surface area, the dA/dlog(W) surface area, the cumulative

549   pore volume and the dV/dlog(W) pore volume as a function of the pore width of AC obtained

550   from runs 2, 3, 6 and DoE validation run.

551
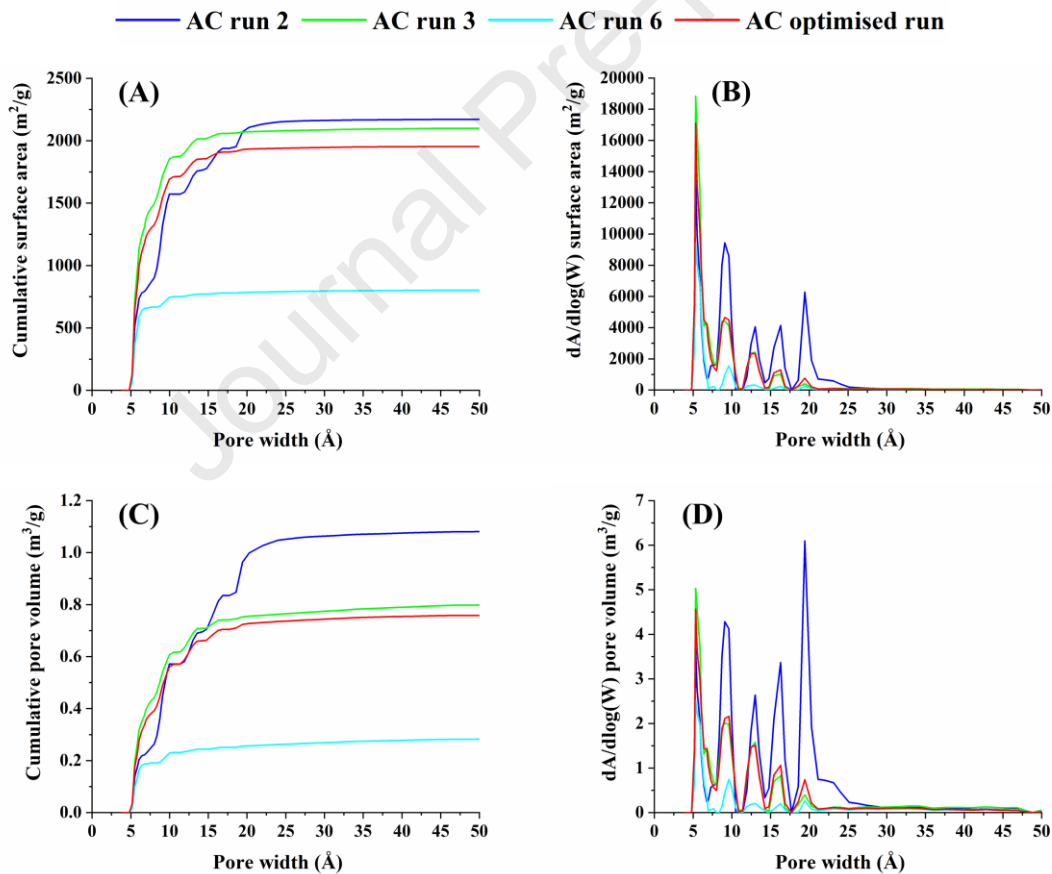
553   **Fig. 6**

554

555   The values of the cumulative micropores volume were 1.0, 0.7, 0.2 and 0.7 cm³/g for runs 2,

556   3, 6 and optimised one, respectively. For run 2 (800 °C, KOH/lignin 3.0 wt/wt), major of the

28

557 micropores was characterised by a width of 9.2, 13.0 and 16.2 Å while the presence of larger

558 micropores of around 19 Å was ascertained, as shown in Figures 6B and 6D. For run 3 (650

559 °C, KOH/lignin 2.6 wt/wt), the most abundant micropores showed a width of 5.2, 9.1 and

560 13.0 Å. The AC produced in run 6 (500 °C, KOH/lignin 3.0 wt/wt) presented micropores of

561 5.3 and 9.6 Å. Lastly, AC obtained under the optimised reaction conditions (630 °C,

562 KOH/lignin 3.0 wt/wt) was characterised by micropores with a width of 5.2, 9.1 and 13.0 Å,

563 confirming the similar microporous structure and pore distribution of AC of run 3. Moreover,

564 the micropores volume (0.7 cm³/g) was significantly higher the those reported in the literature

565 for AC obtained from *Arundo donax* L., ranging from 0.2 to 0.5 cm³/g (Ahmed, 2016; Singh

566 *et al.*, 2017a), demonstrating again the effectiveness of the proposed cascade process.

567 The improvement of the CO_2 uptake requires the enhancement of the microporosity,

568 surface area, and pore volume of the AC. Moreover, AC readily lends itself to the

569 incorporation of surface oxygenated functional groups like carboxylates and hydroxyls,

570 enabling CO_2 capture through processes such as cation exchange, strong complexation, and

571 electrostatic attractions (Azmi *et al.*, 2022). Remarkably, heteroatoms such as sulphur,

572 nitrogen, oxygen, and hydrogen assume a crucial role by interacting specifically with CO_2,

573 leading to improved CO_2 selectivity, and aiding in gas separation. Doping AC with oxygen or

574 utilising raw materials rich in oxygen as precursors facilitates the creation of hydroxyl,

575 carboxylic, and phenol functional groups, which in turn promote CO_2 capture. At the same

576 time, a high concentration of metal oxides can result in pore clogging, ultimately diminishing

577 the performance of CO_2 adsorption (Azmi *et al.*, 2022). Moreover, pores below 10 Å exhibit

578 remarkable selectivity for CO_2 molecules, when present in a N_2/CO_2 mixture (Abd *et al.*,

579 2021). This selectivity arises from their ability to effectively block the passage of N_2

580 molecules through the pore walls. However, pores with dimensions lower than 3.5 Å show

581 reduced adsorption performance because they approach the kinetic diameter of CO_2 molecules

582 (3.3 Å). On the other hand, pores exceeding 10 Å in size are unsuitable for low-pressure CO_2

583 capture, since they may not achieve a sufficiently dense packing of CO_2 molecules (Abd *et*

584 *al.*, 2021). Once having verified the possibility of obtaining AC with a tailored microporosity,

585 it could be possible to further improve its surface properties, depending on the physico-

586 chemical properties of the component to be adsorbed on it. Based on these considerations, the

587 results obtained from the analysis of the specific surface area, pore volume and size

588 distribution of ACs produced in runs 2, 3, 6 and under the optimised conditions (Fig. 5 and 6)

589 were correlated with those obtained from the analysis of CO_2 uptake (Table 7), as well as with

590 those obtained from the elemental analysis (Table 6). The AC produced in run 2 (800 °C,

591 KOH/lignin 3.0 wt/wt) was characterised by the highest values of specific surface area,

592 micropore area, external surface area and cumulative micropores volume, but also by a lower

593 CO_2 uptake (47.0 mg/g) with respect to the values achieved for ACs produced in run 3 (650

594 °C, KOH/lignin 2.6 wt/wt) and under the optimised reaction conditions (630 °C, KOH/lignin

595 3.0 wt/wt), equal to 72.6 and 72.3, respectively. The better adsorbing performances of these

596 last two ACs can be explained by considering the micropore size and distribution (Fig. 6), as

597 well as the oxygen content (Table 6). In fact, ACs produced in run 3 and under the optimised

598 conditions were characterised by the abundance of micropores with a width of 5.2, 9.1 and

599 13.0 Å and by the oxygen content of 18.6 and 18.3 wt%, respectively. Differently, AC

600 produced in run 2 was mainly characterised by larger micropores with a width of 13.0, 16.2

601 and 19 Å and by a lower oxygen content (5.1 wt%) and higher ash content (18.1 wt%). The

602 synergistic effect of these features decreased the selectivity of AC obtained in run 2 and

603 increased that of ACs produced in run 3 and in the optimised run towards the adsorption of

604 CO_2 molecules in the mixture CO_2/N_2, according to the literature (Abd *et al.*, 2021).

605 According to this reasoning, a schematic representation of the CO_2 adsorption mechanism was

606 reported in Figure S7.

607   SEM images of pristine lignin-rich precursor and AC obtained under the optimised process

608   conditions (630 °C, KOH/lignin 3.0 wt/wt, 60 min) are shown in Figure 7.

609
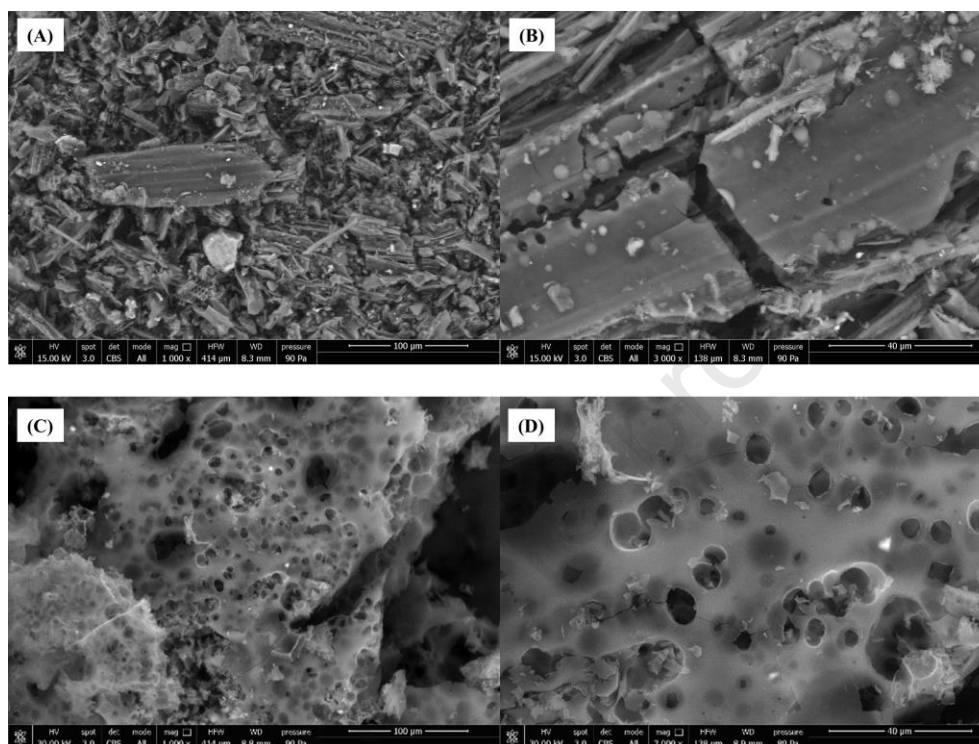
610

611   **Fig. 7**

612

613   The effect of the thermochemical activation was evident since the lignin-rich residue was

614   characterised by a non-porous and flat morphology while AC revealed a rather porous and

615   shrunk structure, with pores diameter <40 µm (Fig. 7D). Moreover, as shown in Fig. 7C, AC

616   was characterised by a uniform distribution of micropores. The morphological features of AC

617   obtained under the optimised process conditions were ascribed to a collapse of the carbon

618   matrix, due to the higher amount of KOH used in the activation protocol (KOH/lignin ratio of

619   3.0 wt/wt), in agreement with the literature findings (Singh *et al.*, 2017a). The high

620   concentration of KOH initiates the carbon walls' breakdown, interconnecting an aligned

621   porous carbon structure, through oxidation at high temperature. Simultaneously, potassium

622   residues produced during the activation process profoundly alter the surface morphology of

31

623 the sample (Nandi *et al.*, 2023). These findings underscored the importance of properly tuning

624 the activation process of ACs, characterised by a uniform morphology, a consistently aligned

625 porous structure, and outstanding surface properties, such as a high specific surface area and
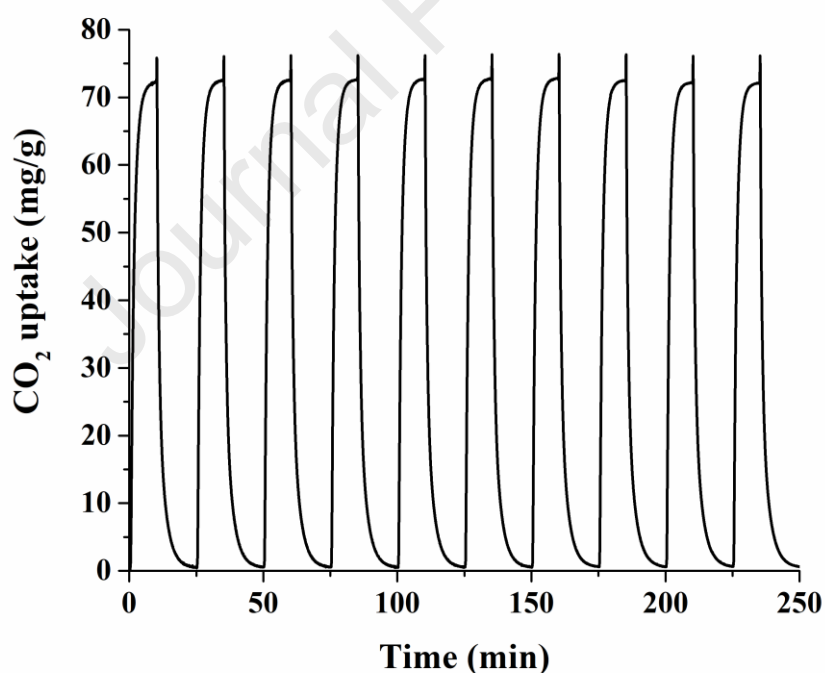
626 micropore volume.

627

628 ### 3.4 Recycling test of activated carbon for CO_2 uptake

629

630 Figure 8 shows 10 adsorption and desorption cycles of CO_2 by the AC obtained under the

631 optimised process conditions.

632

633

634 **Fig. 8**

635

636 Firstly, it is noteworthy that the maximum achieved CO_2 uptake of 72.3 mg/g was obtained by

637 working at a CO_2 partial pressure of 0.60 bar, which is more representative of more real

638 conditions, such as those of post-combustion flue gas. This adsorption performance

639 demonstrated the feasibility of the use of this kind of AC as CO_2 adsorbent for industrial

640 applications. Moreover, the equilibrium time observed in the recycling tests was always very

641 short (ca. 10 min), confirming the good properties and performances of this biomaterial.

642 Lastly, an almost identical trend was ascertained for all the cycles, thus demonstrating that the

643 AC obtained in this study is regenerable and reusable, which are desirable aspects for eventual

644 industrial uses. The prevailing presence of microporosity in the synthesised AC is also

645 desirable for performing solid-liquid adsorption studies, for example, those aimed at the

646 removal of organic pollutants, such as phenol, from wastewaters (Dehmani *et al.*, 2023). On

647 this basis, the use of the synthesised AC for such applications in the liquid phase seems

648 promising and certainly worthy of further attention. These important features significantly

649 increased the sustainability of the implemented approach for the lignin residue valorisation,

650 especially when AC finds application as filter material (Sevilla *et al.*, 2012).

651

3.5 Flow diagram of the proposed biorefinery scheme

653

654 Figure 9 shows the mass flow diagram of the proposed biorefinery scheme, which is based

655 on the MW-assisted conversion of hemicellulose and cellulose into xylose and levulinic acid,

656 respectively. The subsequent step involves upgrading the xylose-rich hydrolysate (XRH) to

657 produce single cell oil (SCO) using the yeast *L. starkeyi*, as discussed in our previous works

658 (Di Fidio *et al.*, 2019; Di Fidio *et al.*, 2020a; Di Fidio *et al.*, 2021a). Finally, the lignin-rich

659 stream is valorised by producing AC under the optimised process conditions presented in this
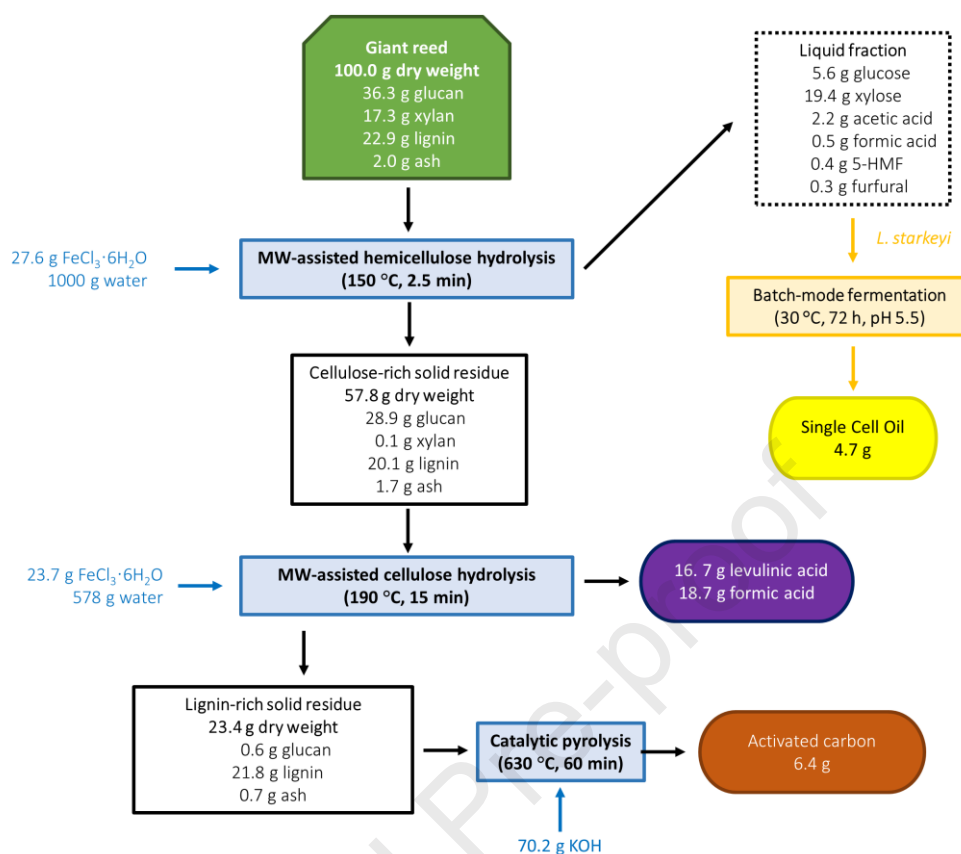
660 study.

661

Fig. 9

Starting from 100 g of *Arundo donax* L., 19.4 g of xylose, 5.6 g of glucose, 16.7 g of levulinic acid and 18.7 g of formic acid were produced. Then, by fermenting the XRH, 4.7 g of SCO was achieved. Moreover, a final lignin-rich stream (23 g), containing 93.2 wt% acid-insoluble lignin, was obtained as the residue of this process, which allows the production of 6.4 g of AC. Lastly, it is important to emphasise the short processing time of the entire biorefinery process proposed in the present study since the first step requires only 2.5 min, the second one 15 min and the last one 60 min. The complete valorisation of the starting raw material and the sustainable reaction conditions adopted in each step significantly improved the sustainability of the cascade process in the perspective of the Green Chemistry principles.

Conclusions

676

677 A new thermochemical route was optimised for closing the cycle of the valorisation of

678 *Arundo donax* L. After the hydrolysis of hemicellulose to xylose and cellulose to levulinic

679 and formic acid, the final lignin-rich residue was characterised and chemically activated by

680 KOH to produce AC, which was exploited for CO_2 adsorption. The chemometric approach

681 was chosen to improve the activation protocol. Under the optimised conditions (630 °C,

682 KOH/lignin 3.0 wt/wt, 60 min) the AC yield was 34.4 wt% and the maximum CO_2 uptake

683 was 72.3 mg/g, kept over 10 cycles of adsorption/desorption tests, demonstrating its feasible

684 regeneration without losing its starting CO_2 uptake capacity. The complete and tailored

685 conversion of the different components of this non-edible biomass represents a step forward

686 in the perspective of green and sustainable biorefinery processes.

687

701

Appendix A. Supplementary data

E-supplementary data of this word can be found in online version of the paper.

704

References

1. Abd, A.A., Othman, M.R., Kim, J., 2021. A review on application of activated carbons for carbon dioxide capture: present performance, preparation, and surface modification for further improvement. Environ. Sci. Pollut. Res. 28, 43329-43364. https://doi.org/10.1007/s11356-021-15121-9.

2. Ahmed, M.J., 2016. Potential of *Arundo donax* L. stems as renewable precursors for activated carbons and utilization for wastewater treatments. J. Taiwan Inst. Chem. Eng. 63, 336-343. https://doi.org/10.1016/j.jtice.2016.03.030.

3. Alcañiz-Monge, J., Román-Martínez, M.d.C., Lillo-Ródenas, M.Á., 2022. Chemical Activation of Lignocellulosic Precursors and Residues: What Else to Consider? Molecules 27, 1630-1655. https://doi.org/10.3390/molecules27051630.

4. Allahkarami, E., Azadmehr, A., Noroozi, F., Farrokhi, S., Sillanpää, M., 2022. Nitrate adsorption onto surface-modified red mud in batch and fixed-bed column systems: equilibrium, kinetic, and thermodynamic studies. Environ. Sci. Pollut. Res. 29, 48438-48452. https://doi.org/10.1007/s11356-022-19311-x.

5. Allahkarami, E., Dehghan Monfared, A., Silva, L.F.O., Dotto, G.L., 2022. Lead ferrite-activated carbon magnetic composite for efficient removal of phenol from aqueous solutions: Synthesis, characterization, and adsorption studies. Sci. Rep. 12, 10718-10733. https://doi.org/10.1038/s41598-022-15077-x.

6. Allahkarami, E., Dehghan Monfared, A., Silva, L.F.O., Dotto, G.L., 2023a. Application of Pb–Fe spinel-activated carbon for phenol removal from aqueous solutions: fixed-bed adsorption studies. Environ. Sci. Pollut. Res. 30, 23870-23886. https://doi.org/10.1007/s11356-022-23891-z.

7. Allahkarami, E., Dehghan Monfared, A., Silva, L.F.O., Dotto, G.L., 2023b. Toward a mechanistic understanding of adsorption behavior of phenol onto a novel activated carbon composite. Sci. Rep. 13, 167-182. https://doi.org/10.1038/s41598-023-27507-5.

8. Allahkarami, E., Soleimanpour Moghadam, N., Jamrotbe, B., Azadmehr, A., 2023. Competitive adsorption of Ni(II) and Cu(II) ions from aqueous solution by vermiculite-

733 alginate composite: batch and fixed-bed column studies. J. Dispers. Sci. Technol. 44,

734 1402-1412. https://doi.org/10.1080/01932691.2021.2017297.

735 9. Asada, C., Sasaki, C., Oka, C., Nakamura, Y., 2020. Ethanol production from sugarcane

736 bagasse using pressurized microwave treatment with inorganic salts and salt-tolerant

737 yeast. Waste Biomass Valorization 11, 2001-2007. https://doi.org/10.1007/s12649-018-

738 0527-z.

739 10. Azmi, N.Z.M., Buthiyappan, A., Raman, A.A.A., Patah, M.F.A., Sufian, S., 2022. Recent

740 advances in biomass based activated carbon for carbon dioxide capture-a review. J. Ind.

741 Eng. Chem. 116, 1-20. https://doi.org/10.1016/j.jiec.2022.08.021.

742 11. Bhattarai, K.P., Pant, B.D., Rai, R., Aryal, R.L., Paudyal, H., Gautam, S.K., Ghimire,

743 K.N., Pokhrel, M.R., Poudel, B.R., 2022. Efficient sequestration of Cr(VI) from aqueous

744 solution using biosorbent derived from *Arundo donax* stem. J. Chem. 2022, 1-12.

745 https://doi.org/10.1155/2022/9926391.

746 12. Chen, B., Wang, X., Leng, W., Mei, C., Zhai, S., 2019. Spectroscopic/Microscopic

747 elucidation for chemical changes during acid pretreatment on *Arundo donax*. J. Bioresour.

748 Bioprod. 4, 192-199. http://dx.doi.org/10.12162/jbb.v4i3.008.

749 13. Constant, S., Wienk, H.L., Frissen, A.E., de Peinder, P., Boelens, R., Van Es, D.S., Grisel,

750 R.J., Weckhuysen, B.M., Huijgen, W.J., Gosselink, R.J., 2016. New insights into the

751 structure and composition of technical lignins: a comparative characterisation study.

752 Green Chem. 18, 2651-2665. https://doi.org/10.1039/C5GC03043A.

753 14. Dehmani, Y., Franco, D.S., Georgin, J., Lamhasni, T., Brahmi, Y., Oukhrib, R., Youcef,

754 H.B., Sadik, A., 2023. Towards experimental and theoretical understanding of the

755 adsorption behavior of phenol on a new activated carbon prepared from oak wood. J.

756 Water Process. Eng. 54, 103936-103947. https://doi.org/10.1016/j.jwpe.2023.103936.

757 15. Di Fidio, N., Antonetti, C., Raspolli Galletti, A.M., 2019. Microwave-assisted cascade

758 exploitation of giant reed (*Arundo donax* L.) to xylose and levulinic acid catalysed by

759 ferric   chloride.   Bioresour.   Technol.   293,   122050-122058.

760 https://doi.org/10.1016/j.biortech.2019.122050.

761 16. Di Fidio, N., Fulignati, S., De Bari, I., Antonetti, C., Raspolli Galletti, A.M., 2020a.

762 Optimisation of glucose and levulinic acid production from the cellulose fraction of giant

763 reed (*Arundo donax* L.) performed in the presence of ferric chloride under microwave

764 heating.   Bioresour.   Technol.   313,   123650-123658.

765 https://doi.org/10.1016/j.biortech.2020.123650.

17. Di Fidio, N., Ragaglini, G., Dragoni, F., Antonetti, C., Raspolli Galletti, A.M., 2021a. Integrated cascade biorefinery processes for the production of single cell oil by *Lipomyces starkeyi* from *Arundo donax* L. hydrolysates. Bioresour. Technol. 325, 124635-124645. https://doi.org/10.1016/j.biortech.2020.124635.

18. Di Fidio, N., Raspolli Galletti, A.M., Fulignati, S., Licursi, D., Liuzzi, F., De Bari, I., Antonetti, C., 2020b. Multi-step exploitation of raw *Arundo donax* L. for the selective synthesis of second-generation sugars by chemical and biological route. Catalysts 10, 79-101. https://doi.org/10.3390/catal10010079.

19. Di Fidio, N., Timmermans, J.W., Antonetti, C., Raspolli Galletti, A.M., Gosselink, R.J., Bisselink, R.J., Slaghek, T.M., 2021b. Electro-oxidative depolymerisation of technical lignin in water using platinum, nickel oxide hydroxide and graphite electrodes. New J. Chem. 45, 9647-9657. https://doi.org/10.1039/D1NJ01037A.

20. Fiore, V., Scalici, T., Valenza, A., 2014. Characterization of a new natural fiber from *Arundo donax* L. as potential reinforcement of polymer composites. Carbohydr. Polym. 106, 77-83. https://doi.org/10.1016/j.carbpol.2014.02.016.

21. Guo, B., Zhang, J., Wang, Y., Qiao, X., Xiang, J., Jin, Y., 2023. Study on CO_2 adsorption capacity and kinetic mechanism of CO_2 adsorbent prepared from fly ash. Energy 263, 125764-125775. https://doi.org/10.1016/j.energy.2022.125764.

22. Heidarinejad, Z., Dehghani, M.H., Heidari, M., Javedan, G., Ali, I., Sillanpää, M., 2020. Methods for preparation and activation of activated carbon: a review. Environ. Chem. Lett. 18, 393-415. https://doi.org/10.1007/s10311-019-00955-0.

23. Horikoshi, S., Minagawa, T., Tsubaki, S., Onda, A., Serpone, N., 2017. Is selective heating of the sulfonic acid catalyst $AC\text{-}SO_3H$ by microwave radiation crucial in the acid hydrolysis of cellulose to glucose in aqueous media? Catalysts 7, 231-243. https://doi.org/10.3390/catal7080231.

24. Iris, K., Tsang, D.C., Yip, A.C., Chen, S.S., Wang, L., Ok, Y.S., Poon, C.S., 2017. Catalytic valorization of starch-rich food waste into hydroxymethylfurfural (HMF): controlling relative kinetics for high productivity. Bioresour. Technol. 237, 222-230. https://doi.org/10.1016/j.biortech.2017.01.017.

25. Jagiello, J., Ania, C., Parra, J.B., Cook, C., 2015. Dual gas analysis of microporous carbons using 2D-NLDFT heterogeneous surface model and combined adsorption data of N_2 and CO_2. Carbon 91, 330-337. https://doi.org/10.1016/j.carbon.2015.05.004.

798   26. Kaur, G., Singh, N., Rajor, A., 2021. Adsorption of doxycycline hydrochloride onto
799   powdered activated carbon synthesized from pumpkin seed shell by microwave-assisted
800   pyrolysis.   Environ.   Technol.   Innov.   23,   101601-101614.
801   https://doi.org/10.1016/j.eti.2021.101601.

802   27. Licursi, D., Antonetti, C., Di Fidio, N., Fulignati, S., Benito, P., Puccini, M., Vitolo, S.,
803   Raspolli Galletti, A.M., 2023. Conversion of the hydrochar recovered after levulinic acid
804   production into activated carbon adsorbents. Waste Manage. 168, 235-245.
805   https://doi.org/10.1016/j.wasman.2023.06.012.

806   28. Loow, Y.L., Wu, T.Y., Tan, K.A., Lim, Y.S., Siow, L.F., Md Jahim, J., Mohammad,
807   A.W., Teoh, W.H., 2015. Recent advances in the application of inorganic salt
808   pretreatment for transforming lignocellulosic biomass into reducing sugars. J. Agric. Food
809   Chem. 63, 8349-8363. https://doi.org/10.1021/acs.jafc.5b01813.

810   29. MacDermid-Watts, K., Pradhan, R., Dutta, A., 2021. Catalytic hydrothermal
811   carbonization treatment of biomass for enhanced activated carbon: a review. Waste
812   Biomass Valorization 12, 2171-2186. https://doi.org/10.1007/s12649-020-01134-x.

813   30. Malini, K., Selvakumar, D., Kumar, N., 2023. Activated carbon from biomass:
814   Preparation, factors improving basicity and surface properties for enhanced CO_2 capture
815   capacity–A   review.   J. CO_2 Util.   67,   102318-102327.
816   https://doi.org/10.1016/j.jcou.2022.102318.

817   31. Maziarka, P., Wurzer, C., Arauzo, P.J., Dieguez-Alonso, A., Mašek, O., Ronsse, F., 2021.
818   Do you BET on routine? The reliability of N_2 physisorption for the quantitative
819   assessment of biochar's surface area. Chem. Eng. J. 418, 129234-129246.
820   https://doi.org/10.1016/j.cej.2021.129234.

821   32. Nandi, R., Jha, M.K., Guchhait, S.K., Sutradhar, D., Yadav, S., 2023. Impact of KOH
822   Activation on Rice Husk Derived Porous Activated Carbon for Carbon Capture at Flue
823   Gas alike Temperatures with High CO_2/N_2 Selectivity. ACS omega 8, 4802-4812.
824   https://doi.org/10.1021/acsomega.2c06955.

825   33. Pilu, R., Cassani, E., Landoni, M., Badone, F.C., Passera, A., Cantaluppi, E., Corno, L.,
826   Adani, F., 2014. Genetic characterization of an Italian Giant Reed (*Arundo donax* L.)
827   clones   collection: exploiting   clonal   selection.   Euphytica   196,   169-181.
828   https://doi.org/10.1007/s10681-013-1022-z.

829   34. Priecel, P., Lopez-Sanchez, J.A., 2018. Advantages and limitations of microwave reactors:

830   from chemical synthesis to the catalytic valorization of biobased chemicals. ACS Sustain.

831   Chem. Eng. 7, 3-21. https://doi.org/10.1021/acssuschemeng.8b03286.

832   35. Qin, H., Jian, R., Bai, J., Tang, J., Zhou, Y., Zhu, B., Zhao, D., Ni, Z., Wang, L., Liu, W.,

833   2018. Influence of molecular weight on structure and catalytic characteristics of ordered

834   mesoporous carbon derived from lignin. ACS Omega 3, 1350-1356.

835   https://doi.org/10.1021/acsomega.7b01870.

836   36. Raspolli Galletti, A.M., Licursi, D., Ciorba, S., Di Fidio, N., Coccia, V., Cotana, F.,

837   Antonetti, C., 2021. Sustainable exploitation of residual *Cynara cardunculus* L. to

838   levulinic   acid   and   *n*-butyl   levulinate.   Catalysts   11,   1082-1099.

839   https://doi.org/10.3390/catal11091082.

840   37. Rezai, B., Allahkarami, E., 2021. Wastewater treatment processes—techniques,

841   technologies, challenges faced, and alternative solutions, in: Karri, R.R., Ravindran, G.,

842   Dehghani, M. H. (Eds.) Soft Computing Techniques in Solid Waste and Wastewater

843   Management. Elsevier, pp. 35-53. https://doi.org/10.1016/B978-0-12-824463-0.00004-5.

844   38. Rouquerol, J., Llewellyn, P., Rouquerol, F., 2007. Is the BET equation applicable to

845   microporous   adsorbents?   Stud.   Surf.   Sci.   Catal.   160,   49-56.

846   https://doi.org/10.1016/S0167-2991(07)80008-5.

847   39. Scordia, D., Cosentino, S.L., 2019. Perennial energy grasses: Resilient crops in a changing

848   European agriculture. Agriculture 9, 169-187. https://doi.org/10.3390/agriculture9080169.

849   40. Sellaoui, L., Gómez-Avilés, A., Dhaouadi, F., Bedia, J., Bonilla-Petriciolet, A., Rtimi, S.,

850   Belver, C., 2023. Adsorption of emerging pollutants on lignin-based activated carbon:

851   Analysis of adsorption mechanism via characterization, kinetics and equilibrium studies.

852   Chem. Eng. J. 452, 139399-139407. https://doi.org/10.1016/j.cej.2022.139399.

853   41. Serafin, J., Narkiewicz, U., Morawski, A.W., Wróbel, R.J., Michalkiewicz, B., 2017.

854   Highly microporous activated carbons from biomass for CO_2 capture and effective

855   micropores   at   different   conditions.   J. CO_2 Util.   18,   73-79.

856   https://doi.org/10.1016/j.jcou.2017.01.006.

857   42. Sevilla, M., Falco, C., Titirici, M.M., Fuertes, A.B., 2012. High-performance CO_2

858   sorbents   from   algae.   RSC   Adv.   2(33),   12792-12797.

859   https://doi.org/10.1039/C2RA22552B.

43. Singh, G., Kim, I.Y., Lakhi, K.S., Srivastava, P., Naidu, R., Vinu, A., 2017a. Single step synthesis of activated bio-carbons with a high surface area and their excellent CO_2 adsorption capacity. Carbon 116, 448-455. https://doi.org/10.1016/j.carbon.2017.02.015.

44. Singh, G., Lakhi, K.S., Kim, I.Y., Kim, S., Srivastava, P., Naidu, R., Vinu, A., 2017b. Highly efficient method for the synthesis of activated mesoporous biocarbons with extremely high surface area for high-pressure CO_2 adsorption. ACS Appl. Mater. Interfaces 9, 29782-29793. https://doi.org/10.1021/acsami.7b08797.

45. Sluiter, A., Hames, B., Ruiz, R., Scarlata, C., Sluiter, J., Templeton, D., Crocker, D., 2008. NREL/TP-510–42618 1617, 1-16.

46. Song, T., Liao, J.M., Xiao, J., Shen, L.H., 2015. Effect of micropore and mesopore structure on CO_2 adsorption by activated carbons from biomass. New Carbon Mater. 30, 156-166. https://doi.org/10.1016/S1872-5805(15)60181-0.

47. Supanchaiyamat, N., Jetsrisuparb, K., Knijnenburg, J.T., Tsang, D.C., Hunt, A., 2019. Lignin materials for adsorption: Current trend, perspectives and opportunities. Bioresour. Technol. 272, 570-581. https://doi.org/10.1016/j.biortech.2018.09.139.

48. Üner, O., 2019. Hydrogen storage capacity and methylene blue adsorption performance of activated carbon produced from *Arundo donax*. Mater. Chem. Phys. 237, 121858-121868. https://doi.org/10.1016/j.matchemphys.2019.121858.

49. United Nations, 2023. Sustainable Development Golas https://www.un.org/sustainabledevelopment/ (accessed 30-08-2023).

50. Viccaro, M., Caniani, D., Masi, S., Romano, S., Cozzi, M., 2022. Biofuels or not biofuels? The "Nexus Thinking" in land suitability analysis for energy crops. Renew. Energy 187, 1050-1064. https://doi.org/10.1016/j.renene.2022.02.008.

51. Xing, L.A., Yang, F., Zhong, X., Liu, Y., Lu, H., Guo, Z., Lv, G., Yang, J., Yuan, A., Pan, J., 2023. Ultra-microporous cotton fiber-derived activated carbon by a facile one-step chemical activation strategy for efficient CO_2 adsorption. Sep. Purif. Technol. 324, 124470-124480. https://doi.org/10.1016/j.seppur.2023.124470.

52. Yagmur, E., Gokce, Y., Tekin, S., Semerci, N.I., Aktas, Z., 2020. Characteristics and comparison of activated carbons prepared from oleaster (*Elaeagnus angustifolia* L.) fruit using KOH and $ZnCl_2$. Fuel 267, 117232-117239. https://doi.org/10.1016/j.fuel.2020.117232.

891   53. You, T.T., Mao, J.Z., Yuan, T.Q., Wen, J.L., Xu, F., 2013. Structural elucidation of the
892   lignins from stems and foliage of *Arundo donax* Linn. J. Agric. Food Chem. 61, 5361-
893   5370. https://doi.org/10.1021/jf401277v.

894   54. Zulkania, A., Hanum, G.F., Rezki, A.S., 2018. The potential of activated carbon derived
895   from bio-char waste of bio-oil pyrolysis as adsorbent, MATEC Web of Conferences. EDP
896   Sciences, pp. 01029-01034. https://doi.org/10.1051/matecconf/201815401029.

Highlights

- The biorefinery of lignocellulosic *Arundo donax* L. biomass was completed.

- Microporous activated carbon was obtained from the residual lignin-rich fraction.

- A chemometric approach was used to optimise the production of activated carbon.

- Yields in activated carbon and carbon were 34.4 and 40.6 wt%, respectively.

- The CO_2 uptake was 7.2 wt%, kept over 10 cycles of adsorption/desorption.

CRediT authorship contribution statement

Nicola Di Fidio: Conceptualization, Methodology, Investigation, Formal analysis, Writing - original draft. **Domenico Licursi:** Formal analysis, Writing - review & editing. **Monica Puccini:** Conceptualization, Methodology, Formal analysis, Writing - review & editing, Funding acquisition.

Sandra Vitolo: Writing - review & editing, Resources. **Anna Maria Raspolli Galletti:** Writing - review & editing, Supervision, Funding acquisition.

Declaration of interests

☒ The authors declare that they have no known competing financial interests or personal relationships that could have appeared to influence the work reported in this paper.

☐ The authors declare the following financial interests/personal relationships which may be considered as potential competing interests: